Formation of two glass phases in binary Cu-Ag liquid

Qi An[a,*], William L. Johnson[b,*], Konrad Samwer[c], Sydney L. Corona[b], William A. Goddard III[d,*]

[a] *Department of Chemical and Materials Engineering, University of Nevada-Reno, Reno, Nevada 89557, United States*
[b] *Keck Engineering Laboratories, California Institute of Technology, Pasadena, CA 91125, United States*
[c] *I. Physikalisches Institut, University of Goettingen, 37077 Goettingen, Germany*
[d] *Materials and Process Simulation Center, California Institute of Technology, Pasadena, CA 91125, United States*

ABSTRACT

The glass transition is alternatively described as either a dynamic transition in which there is a dramatic slowing down of the kinetics, or as a thermodynamic phase transition. To examine the physical origin of the glass transition in fragile Cu-Ag liquids, we employed molecular dynamics (MD) simulations on systems in the range of 32,000 to 2,048,000 atoms. Surprisingly, we identified a 1st order freezing transition from liquid (L) to metastable heterogenous solid-like phase, denoted as the G-glass, when a supercooled liquid evolves isothermally below its melting temperature at deep undercooling. In contrast, a more homogenous liquid-like glass, denoted as the L-glass, is achieved when the liquid is quenched continuously to room temperature with a fast cooling rate of ~10^{11} K/*sec*. We report a thermodynamic description of the L-G transition and characterize the correlation length of the heterogenous structure in the G-glass. The shear modulus of the G-glass is significantly higher than the L-glass, suggesting that the first order L-G transition is linked fundamentally to long-range elasticity involving elementary configurational excitations in the G-glass.

© 2020 Acta Materialia Inc. Published by Elsevier Ltd. All rights reserved.

1. Introduction

The glass transition occurs as a liquid is rapidly quenched to a deeply undercooled state and configurationally freezes without intervention of crystallization. This transition is accompanied by a loss of the configuration entropy of the liquid [1–3]. Glasses are formed in chemically diverse substances including organic oxides [4], organic polymers [5], molecular liquids [6], and metallic systems [7–9]. They are ubiquitous in our daily life with important technological and industrial applications owing to their desirable and unique physical and mechanical properties distinct from crystalline materials [10,11]. In his pioneering work, Goldstein proposed that the occurrence of the glassy state is intrinsically related to the existence of potential energy barriers, large compared to thermal energy [12], that separate stable liquid configurations. The configurational entropy of a supercooled liquid is defined as $S_C = \ln W_C(\phi)$, where W_C is the density of stable configurations or inherent states, depending on the configurational potential energy per atom, ϕ. This forms the potential energy landscape (PEL) theory [13–17] and provides the basis for describing the glass transitions from the perspective of thermodynamics.

From the kinetics point of view, a glass "transition" occurs as a liquid becomes more viscous with a significant increase of relaxation time near the glass transition temperature, T_g [18]. The dynamical heterogeneity that characterizes structural relaxation in liquids has been investigated extensively [18–20]. Indeed, numerous experimental and theoretical studies have suggested the possible existence of an underlying thermodynamic glass transition [21–33]. Experimentally, several metastable undercooled liquid phases may exist, leading to the liquid-liquid phase transitions (LLPT's) [21–29]. Particularly, very recent experiments showed that multiple critical cooling rates could generate different types of metallic glasses [34]. Theoretically, recent molecular dynamics (MD) simulations provide some evidence for the thermodynamic nature of the glass transition [35,36]. An et al. showed from MD simulations that undercooled liquid Ag undergoes a first-order configurational freezing transition from the high-temperature homogeneous disordered liquid phase to a metastable, heterogeneous, configurationally ordered phase referred to as the G-phase [36]. This phase exhibits a strong first order melting behavior upon rapid heating, very different from the traditional view of the glass transition [36,37].

In this Article, we employed large-scale MD simulations to investigate glass formation on quenching of binary Ag-Cu liquids with various compositions spanning from Ag rich to Cu rich regions. As the binary Cu-Ag liquids are ultrafast quenched to room temperature with cooling rates between $3.4 \times 10^{10} \sim 3.4 \times 10^{12}$ K/*sec*, the liquids freeze configurationally to a glass that exhibits homogeneous liquid-like character, which we denote as the L-glass. To examine the thermodynamics and metastability of undercooled liquids, we performed the isothermal MD simulations and relaxed the binary Cu-Ag liquids at 700 K for over 10 nanoseconds. Surprisingly, we observed a sharp enthalpy drop and

entropy jump as the liquid transforms to a heterogeneous glassy phase, suggesting a first-order phase transition. The spatial distribution of configurational enthalpy within the product glass phase, denoted as a G-glass, shows an inherently heterogeneous character with a characteristic length scale, Λ. Both Λ and latent heat of L-G transition are correlated with the chemical variations in binary Cu-Ag alloys, suggesting that chemical mixing plays an essential role in this L-G transition. Compared to the L-glass, the G-glass exhibits robust elastic rigidity with a higher finite shear modulus, $\mu(T)$. This underlying mechanism of L-G transition was discussed and may be related to the persistent long-range elasticity in the G-glass.

2. Computational simulation details

2.1. Model construction and MD simulations

To examine the glass transition in binary Cu-Ag systems, the MD simulations were performed using the classical MD code LAMMPS [38] and a Cu-Ag embedded atom model (EAM) potential [39] was applied to describe the interatomic interactions. We used the velocity Verlet algorithm for the integration of equation of motion and a timestep of 1.0 fs in all simulations. The possible surface effects were eliminated by applying periodic boundary conditions (PBC) along all three directions. To illustrate the glass transition as a function of composition, we examined glass formation at eight compositions from Ag rich to Cu rich regions, including $Cu_{100}Ag_0$, $Cu_{80}Ag_{20}$, $Cu_{75}Ag_{25}$, $Cu_{54}Ag_{46}$, $Cu_{30}Ag_{70}$, $Cu_{20}Ag_{80}$, Cu_5Ag_{95}, and Cu_0Ag_{100}. The $Cu_{75}Ag_{25}$ is selected for detailed analyses of the first order L-G transition, thermodynamics functions, and elastic rigidity.

The fast quenching simulations were used for the liquid to L-glass transition. Here, we melted the fcc Ag-Cu crystals at 2000 K and then quenched the liquids to ambient conditions using the cooling rates from 3.4×10^{10} to 3.4×10^{12} K/sec. This process produces the L-glass in all concentrated alloys or crystalline solids in the cases of pure metals or dilute alloy compositions of $Cu_{100}Ag_0$, Cu_5Ag_{95}, and Cu_0Ag_{100}. The G-glass is then produced in the concentrated alloys by isothermally aging the supercooling liquids at 700 K for all compositions, except for the eutectic composition $Cu_{54}Ag_{46}$, which does not spontaneously form the G-glass in the MD timescale. The supercooled liquids at 700 K were obtained from previous liquid to L-glass quenching simulations. To account for the stochastic nature of glass formation (versus crystallization) from liquid, we performed multiple simulations at 700 K with the same liquid structure. The initial condition for the same liquid structure was modified by assigning different velocity distributions. The random seeds were used to produce various Maxwell-Boltzmann distributions at the same temperature. Following isothermal aging, the G-glass was then quenched to room temperature with the same cooling rate used to produce the L-glass. The G-glass at composition $Cu_{75}Ag_{25}$ was remelted by heating back to 2000 K using a heating rate of 3.4×10^{12} K/sec. In all simulations, we apply the isothermal−isobaric (NPT) ensemble to account for the volume changes during glass formation or remelting. To maintain constant temperature and pressure in NPT, we used the Nose-Hoover thermostat and barostat with the damping constants of 100 fs and 1000 fs, respectively. The thermodynamic properties, such as entropy, potential energy and free energy, are derived from equilibrium MD simulations for all present phases including liquid (L), L-glass, G-glass, crystal (X), and mixed crystal state. To examine the size effect, we applied various sizes of systems from 32,000 atoms to 2,048,000 atoms.

2.2. Two-phase simulations to determine G-glass melting temperature and promote G-glass nucleation

To obtain the equilibrium glass melting temperature of the G-glass ($T_{G,M}$), we applied two-phase simulations in which a liquid phase is combined with G-glass phase [40] to form an initial two phases model. Since the liquid phase is homogenous, its dimensions could be adjusted so that it has the same cross section as the G-glass. Then we combined both phases that have the same cross section. In the combined model, these two phases are separated by the average atomic distance in both liquid and G-phase. There are two interfaces in the combined model due to the periodic boundary condition. Several two phase models were constructed at different temperatures from below $T_{G,M}$ to above $T_{G,M}$. Finally, these models were equilibrated at their constructed temperature and the NPT ensemble was used for isothermal equilibration MD runs. If the simulated temperature is above $T_{G,M}$, the two-phase model evolves to a liquid phase eventually, which is indicated by the increased potential energy. In comparison, as the temperature is below $T_{G,M}$, the G-glass phase propagates into the liquid phase, as indicated by the decreased potential energy. The two-phase simulations for the $Cu_{75}Ag_{25}$ composition are displayed in Fig. 1. The crystal melting temperature $T_{X,M}$ = 1050 K for $Cu_{75}Ag_{25}$ was obtained from previous literature [39].

For the eutectic composition $Cu_{54}Ag_{46}$, the G-glass does not nucleate in 100 nanoseconds for MD runs at various supercooled temperatures from 700 K to 900 K. To promote the G-glass formation in MD simulations, we applied the above two-phase simulations by combining the liquid $Cu_{54}Ag_{46}$ with the $Cu_{30}Ag_{70}$ G-glass at 800 K. After 20 ns simulations, the G-glass nucleates from liquid $Cu_{54}Ag_{46}$. Then we replaced the $Cu_{30}Ag_{70}$ G-glass with another liquid $Cu_{54}Ag_{46}$ and continued another 20 nanosecond MD simulation until the whole eutectic system transforms to the G-glass.

2.3. Monte Carlo simulation to obtain the random solid solution (RSS) structure

The random solid solution (RSS) structures were constructed using the Monte Carlo approach. Firstly, we constructed a 32,000 atom fcc lattice and randomly distribute Cu and Ag atoms based on
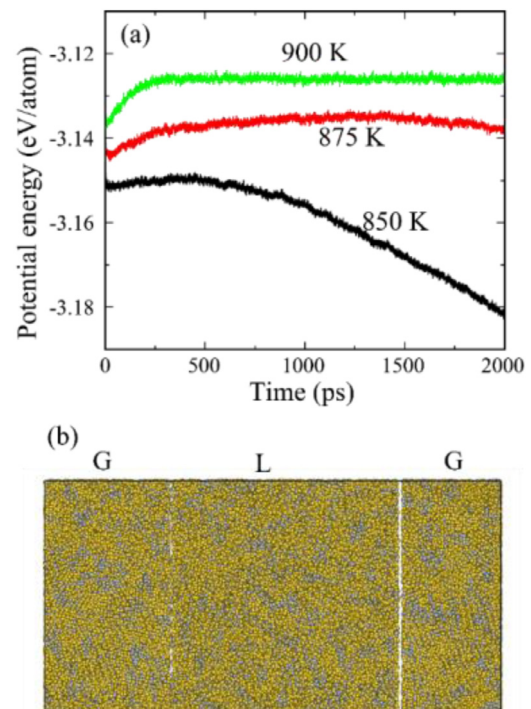

Fig. 1. Two phase coexistence L-G simulations to determine the equilibrium melting temperature $T_{G,M}$ of G-phase $Cu_{75}Ag_{25}$: (a) potential energy evolution of two phase simulations at various temperatures; (b) Two-phase simulation model at 0 ps.

their composition ratios. Then the NPT Monte Carlo (MC) simulations were performed by swapping 10 pairs of atoms in each step at room temperature. A million steps were performed for the potential energy convergence of the MC simulations.

2.4. Honeycut−Anderson (HA) analysis

To characterize the local atomic order in both L-phase and G-phase glasses, we applied the topological Honeycut-Anderson (HA) analysis by considering the geometrical relationship between neighboring pairs of atoms [41]. The local atomic order can be identified by fcc, hcp, and icosahedral types of atoms using HA indices, 1421, 1422 and 1551 [41]. Other disordered or liquid atoms could be described by other types of HA indices such as 1311, 2331, etc. The nearest neighbor and the second nearest neighbor distances were determined using the 1st minimum and the 2nd minimum positions in radial distribution function (RDF), respectively.

2.5. Potential energy (PE) density maps and PE pair distribution function calculations

To separate the configurational enthalpy from the vibrational contribution, we averaged the potential energy (PE) of each atom over a time period of 2 ps, leading to atomic PE density maps. The vibrational motion was averaged over a much longer time (2 ps) than the MD timestep, but sufficiently short compared to configuration relaxation. Therefore, the vibrational noise is removed and the configurational contribution is revealed from PE-density maps.

To determine the average size of the low PE regions, we used the PE pair distribution function (PE-pdf) analysis. We first calculate the average PE/atom ($<PE>$) for Cu and Ag atoms, respectively. Then we compute the mean variance of the PE/atom for each atom type: $\sigma^2 = (1/N)(PE(i)-<PE>)^2$ where i labels the atomic id, as well as the deviation from the average PE for each atom: PE_ave(i) = (PE(i)-$<PE>$). Next, we calculate the dimensionless normalized product: (PE_ave(i) × PE_ave(j)) / σ^2 for every pair of atoms labeled by (i,j). Each pair is separated by the distance $r= r_{ij}=|\mathbf{r}_j-\mathbf{r}_i|$ and the pairs fall into shells along r. Finally, we sum the normalized product over the shells from r to r+dr to generate the PE-pdf correlation function C(r). The C(r) is normalized by dividing it by "$4\pi r^2(N/V)$", as the radial distribution function. This function decreases in amplitude with r and it goes to zero at large distance much greater than correlation length Λ. The correlation length Λ is defined as the C(r) reaches its first minimum value where C(r) becomes negative.

2.6. Shear modulus calculations

Shear modulus may be used to represent the elastic rigidity of both liquid and glass phases. Here we derived the shear modulus from the elastic constants C_{ij} and stiffness constants S_{ij} using the Voigt-Reuss-Hill average [42]. Firstly, we computed elastic constant matrix C_{ij} by deforming the lattice elastically along all possible directions [43]. Then we computed the inverse of elastic matrix Cij and obtained the compliance constant $S_{ij} = (C_{ij})^{-1}$. Finally, the shear modulus is derived by averaging Voigt bounds and Reuss bounds. We performed a 10 ps equilibrium run after the system is deformed before measuring the average stress tensor at various temperatures. The fluctuation of stress is used to compute the statistic errors in predicting shear modulus.

3. Results and discussion

3.1. Glass formation from binary Cu-Ag metallic liquids

We selected the binary Cu-Ag system as a prototype system for studying the glass transition because of its relatively simple phase diagram with no intermetallic compounds present [44]. The influence of

chemical mixing on the glass transition is illustrated by examining several compositions from Cu rich to Ag rich regions: $Cu_{80}Ag_{20}$, $Cu_{75}Ag_{25}$, $Cu_{54}Ag_{46}$, $Cu_{30}Ag_{70}$, $Cu_{20}Ag_{80}$, and Cu_5Ag_{95}. According to previous MD simulations [39], the eutectic composition in our binary Cu-Ag system is $Cu_{54}Ag_{46}$ which is close to the experimental eutectic composition of $Cu_{41}Ag_{59}$ [44]. To investigate glass transition, we first performed quenching simulations from 2000 K to 300 K, as in previous MD studies [45,46], to freeze the 32,000-atom liquid structures using an ultrafast cooling rate of 3.4×10^{12} K/sec. In contrast, we then performed isothermal simulations at 700 K on the supercooled liquids obtained from the quenching simulations to examine their metastability.

Here we use the $Cu_{75}Ag_{25}$ composition to illustrate the characteristics of glass transition, which are similar to those exhibited by most of the other compositions. The eutectic composition $Cu_{54}Ag_{46}$ was not selected because the liquid does not transform to the G-phase within the MD timescales (details discussed below). Fig. 2(a) displays the potential energy per atom, $\phi(T)$, as a function of temperature during quenching. Another lower cooling rate of 3.4×10^{10} K/sec was also applied to illustrate the effects of cooling rate. The glass transition is characterized by the inflection in the $\phi(T)$ cooling curve at ~700 K. Crystallization is not observed in this quenching process as confirmed by the liquid-like radial distribution function (RDF) (Fig. 2b) after quenching with an atomic structure shown in Fig. 2(c). This quenched glass is designed as liquid-like glass or L-glass.

For the quenched liquid held isothermally at 700 K, the $\phi(T)$ shown in Fig. S1 of Supplementary Materials (SM) indicates that the liquid reaches equilibrium within the first ~200 ps and then remains in this equilibrated liquid state for several nanoseconds. The liquid then abruptly undergoes a transition to a new glassy state within a few nanoseconds. Based on the rather abrupt change in $\phi(T)$, this new phase arises from a first order liquid-glass transition that is different from the L-glass. To compare with the L-glass, this G-glass was quenched from 700 K to 300 K using the same quenching rate of
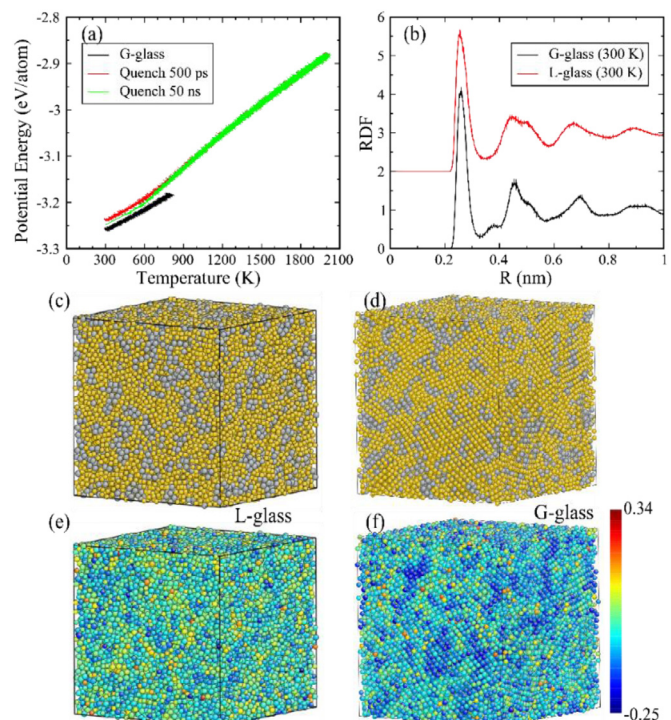

Fig. 2. MD simulations of L-Glass and G-glass formation from a binary $Cu_{75}Ag_{25}$ liquid, including their structural properties: (a) L-glass formation through direct quenching from 2000 K to 300 K and G-glass formation through isothermal MD at *T* = 700 K with subsequent cooling to room temperature; (b) RDF of both G-glass and L-glass at 300 K; (c,d) Atomic structures of both L-glass (c) and G-glass (d) at 300 K; (e,f) PE density map of both L-glass (e) and G-glass (f) at 300 K.

3.4×10^{12} K/*sec*. As shown in Fig. 2(b), the G-glass also displays no long-range order, indicating that it is not a crystalline phase. However, the 2nd peak of the RDF, representing the distance between atoms at opposite vertices of an octahedron, is sharper compared to the L-glass, indicating the short-range order is drastically different from L-glass. The atomic configuration of this G-glass (Fig. 2d) displays locally ordered structures with curved atomic planes that are surrounded by more disordered regions. To distinguish the G-glass from L-glass, we report atomic potential energy (PE) density maps that reveal the spatial distribution of configurational enthalpy within the system. As shown in Fig. 2(e,f), the G-glass exhibits clear heterogenous structure with local ordered structures exhibiting lower PE/atom surrounding by disordered regions with higher PE/atom. In contrast, the L-glass displays a significantly more homogenous character. To further establish the glassy nature of the G-phase, we computed the X-ray powder diffraction (XRD) of both L-glass and G-glass at 300 K, as shown in Fig. S2 of SM. The XRD of L-glass and G-glass are quite similar and lack any evidence of crystalline diffraction peaks indicating long ranger order. A second exemplary L-G transition occurring in the $Cu_{30}Ag_{70}$ liquid exhibits the same characteristics as in the $Cu_{75}Ag_{25}$ system, as shown in Fig. S3 of SM.

The HA analysis [41] was used to further characterize the local atomic structures and the results are displayed in Table 1. The local ordered structure in heterogenous G-glass is revealed by the HA indices of 1421 (40.94%) and 1422 (14.44%) that correspond to local fcc and hcp crystal structures. In comparison, the HA indices in homogenous L-phase are mainly 1551 (25.71%) and 1541 (21.43%) that correspond to icosahedral clusters, along with much less 1421 (5.23%) and 1422 (9.83%). Some icosahedral local structures also appear in the G-glass with the typical indices of 1541 (13.59%) and 1551 (2.35%). On the basis of HA analysis, atoms with fcc and hcp atomic coordination environments were determined for both G-glass and L-glass. As shown in Fig. 3, there are ~19.3% fcc and 5.26% hcp atoms in the G-glass, but only 0.13% fcc and hcp atoms in the L-glass, indicating that the G-glass has significantly more local ordered character than the L-glass. The overall small concentration of fcc and hcp atoms in the G-glass (~1/4 of all atoms) indicates that the G-glass is clearly distinct from a close-packed crystalline phase.

To examine the reversibility of L-G transition, we remelted both glass phases with a heating rate of 3.4×10^{12} K/*sec*. Fig. S4 displays reheating curves for both G-glass and L-glass. The L-glass ϕ(T)-curve shows a more gradual and continuous change as it transforms back to liquid at ~800 K. The G-glass transforms to the liquid at a higher temperature (~1000 K) with a more abrupt change of ϕ(T), suggesting a strong first order melting transition for the G-glass. It is interesting to note that the melting of L-glass occurs at ~800 K which is slightly higher than its glass transition temperature (~700 K) although the L-glass does not exhibit a sharp first order phase transition.

3.2. Latent heat of L-G transition and thermodynamic functions of G-phase

Latent heat represents the energy released or absorbed during a first-order phase transition at fixed pressure (P). To confirm that the L-G transition is a first order phase transition, we computed the latent heat of this transition for the various Ag-Cu compositions, as shown in Fig. 4(a). Data for the elemental one component Ag and Cu systems are also included. We used a large supercell with 2,048,000 atoms for pure Ag and Cu to avoid crystallization arising from a small simulation cell. An L-G transition occurs for all compositions with the exception of the eutectic composition $Cu_{54}Ag_{46}$. For the eutectic system, a 100-nanosecond simulation was performed without observing the transition, indicating that the waiting time for the L-G transition is beyond that accessible to MD. Therefore, we carried out two-phase simulations to produce the G-phase at the eutectic by combining the G-phase of $Cu_{30}Ag_{70}$ with the liquid $Cu_{54}Ag_{46}$ to promote the G-phase nucleation for the eutectic liquid. The latent heat for L-G transition is

Table 1
The Honeycutt-Andersen (HA) indices of two glass phases for the composition $Cu_{75}Ag_{25}$.

HA indices	G-phase	L-phase
1551	2.35%	25.71%
1421	40.94%	5.23%
1422	14.44%	9.83%
1541	13.59%	21.43%
1311	6.82%	4.11%
Others	21.86%	33.69%

found to decrease significantly to 20 ~ 30 meV/atom in the concentrated binary alloys compared to pure Ag and Cu cases (~70 meV/atom). This suggests that the first order character of the L-G transition is significantly suppressed by the chemical mixing. To form the local ordered structure in the G-glass, local chemical separation of Cu and Ag atoms in binary alloys is apparently required, where the waiting time for the L-G transition increases as the composition approaches the eutectic composition.

In order to illustrate the underlying thermodynamic principles of L-G transition, we performed thermodynamic analyses on the liquid and G-phase. The application of equilibrium thermodynamics to study the L-G transition is plausible owing to the robust metastability of both the liquid and G-glass below its melting temperature. The liquid phase in $Cu_{75}Ag_{25}$ persists for several nanoseconds prior to transforming to G-glass and the G-glass remains stable for at least 10 nanoseconds in our simulations. Therefore, we consider the thermodynamic functions for the three phases: crystal (X), liquid (L) and G-glass (G). Since no intermetallic compounds are known for the Ag-Cu binary alloys, two limiting cases of the crystal structures are considered: (1) the physical mixing of pure Ag and pure Cu (mix-X); and (2) a random Ag-Cu fcc solid solution (RSS) phase which is constructed using a Monte Carlo (MC) technique.

The potential energy of the various phases is the sum of a vibrational and a configurational term. Assuming metastable equilibrium at each T, the average vibrational potential energy per atom has the form $\phi^v_\chi(T) = 3/2RT + aT^2 + \ldots$ that includes the classic Dulong-Petit contribution (3/2 RT) and anharmonic terms (the second + higher order terms). The anharmonic terms are generally smaller. For a given phase χ (L, G, RSS or mix-X), we designate $\phi^C_\chi(T)$ as the configurational potential energy as a function of T while the pressure remains zero. For the L-phase, we only consider the states above 800 K since it takes a longer time (>30 ps) for the L-phase to reach equilibrium below T = 800 K. We assume an additional configurational "1/T" term for the liquid phase assuming the configurational entropy of liquid at high T follows the behavior expected for a
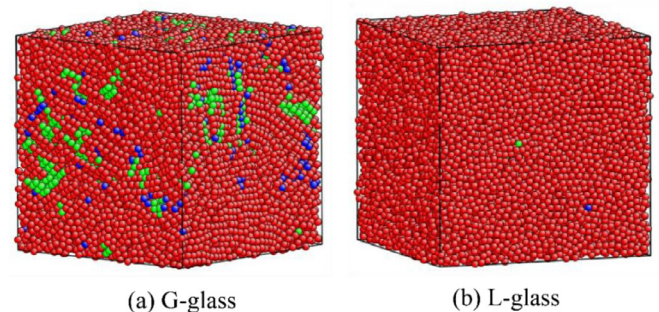

(a) G-glass   (b) L-glass

Fig. 3. The Honeycutt-Anderson analysis on the G-glass and L-glass of $Cu_{75}Ag_{25}$. The G-glass contains 19.3% fcc and 5.26% hcp atoms while the L-glass just have 0.13% fcc+hcp atoms. The fcc, hcp and other atoms are represented by green, blue and red balls, respectively. (For interpretation of the references to colour in this figure legend, the reader is referred to the web version of this article.)
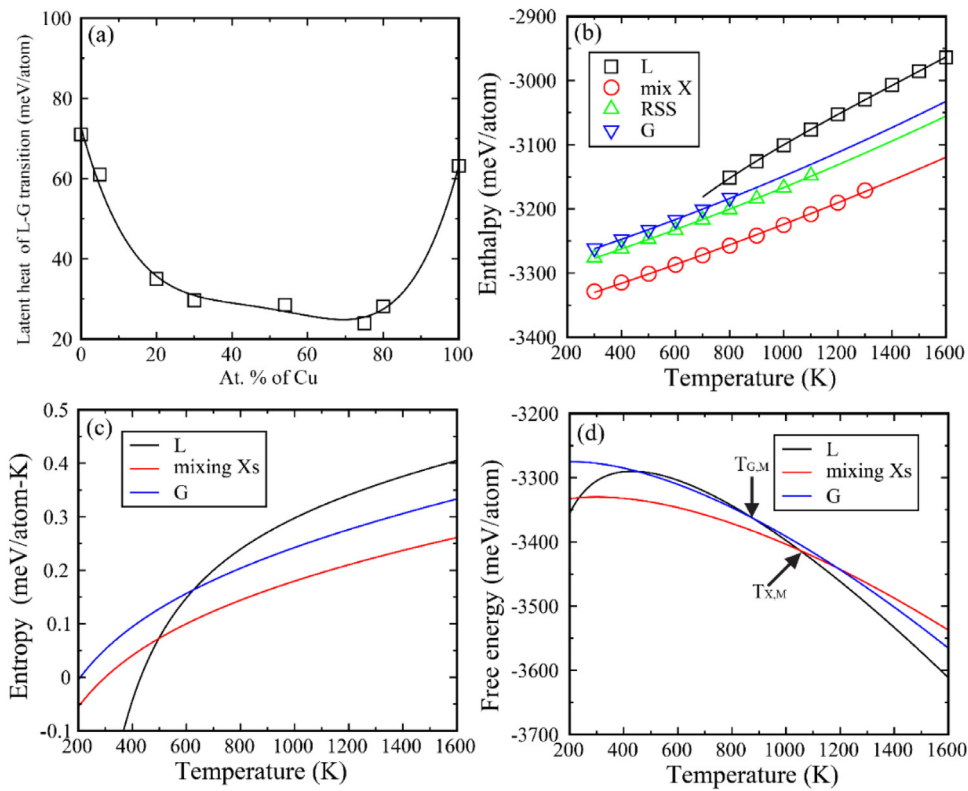
Fig. 4. (a). latent heat of ʟ-G transitions for various compositions at 700 K; (b-d) Enthalpy (b) entropy (c) and Free energy (d) maps of Cu$_{75}$Ag$_{25}$ extracted from MD simulations.

Gaussian distribution of liquid inherent states [47]. This analysis is approximate since the configurational enthalpy of the non-liquid phases was treated as the summation of vibrational terms and an additive constant.

$$\phi_L(T) = -3173.18 \text{mV/atom} + 0.1293\,T + 1.9699 \times 10^{-5} T^2$$
$$- 75950.4/T \tag{1}$$

$$\phi_G(T) = -3303.03 \text{ mV/atom} + 0.1293\,T + 2.48789 \times 10^{-5} T^2 \tag{2}$$

$$\phi_{mX}(T) = -3370.42 \text{ mV/atom} + 0.1293\,T + 1.7236 \times 10^{-5} T^2 \tag{3}$$

$$\phi_{RSS}(T) = -3317.53 \text{ mV/atom} + 0.1293\,T + 2.15926 \times 10^{-5} T^2 \tag{4}$$

The enthalpy (h) curves for various phases are shown in Fig. 4(b) with the $\phi^v(T)$ functions listed in the Eqs. (1−4). The enthalpy of the G-glass is slightly higher than the RSS phase, but they both are much higher in energy than a physical mixture of elemental fcc Ag and Cu. The predicted enthalpy of formation for the Cu-Ag alloys is consistent with experimental measurements [48], validating our approach to predict enthalpy. Since the mix-X phase is the approximate ground state for the crystal at low T (as indicated by the low mutual solubility of Ag and Cu at low T), we considered only the mix-X, G and L in the subsequent entropy and free energy calculations.

The entropy curves were derived by integration of dh/T, as shown in Fig. 4(c). The integration constants were determined by the condition that the free energies are the same for X and L at their melting temperature $T_{X,M}$, the free energies are also the same for G and L at their coexistence temperature, $T_{G,M}$. The entropy of crystal was set to zero at room temperature and was used as the reference state for computing the entropy of other phases. The $T_{X,M}$ was obtained from the experimental phase diagram [44] and the $T_{G,M}$ was determined from the two-phase coexistence simulations (Fig. 1). The specific Gibbs free energy of L, G, and X phases (at $P = 0$) was derived using

the formula, $g = h-Ts$, and the results are displayed in Fig. 4(d). Thus, we obtained all thermodynamic state functions at zero pressure for these three phases. The same approach was also applied to obtain the thermodynamic state functions for the eutectic composition Cu$_{54}$Ag$_{46}$, as displayed in Fig. S5 of SM.

3.3. Structure of the G-phase from PE density maps and the correlation length in G-phase

The G-glass exhibits a heterogenous character with a characteristic length scale, Λ, compared to the homogenous ʟ-glass. To illustrate how the heterogenous structure varies as the composition changes, we computed the PE density maps of metastable G-glass at 700 K for the three compositions Cu$_{75}$Ag$_{25}$, Cu$_{54}$Ag$_{46}$, and Cu$_{20}$Ag$_{80}$. As shown in Fig. 5(a-c), the PE spatial maps reveal a clear heterogeneous structure consisting of low PE ordered regions (dark blue) completely surrounded by the high PE disordered regions (yellow/green). Some curvature is observed in the local atomic planes within the ordered regions, suggesting that either chemical order or "plastic" defects may accommodate the curvature due to the incompatibility of neighboring low PE ordered regions. The ordered regions are topologically isolated and surrounded by the disordered regions with consistently higher PE. Thus, the structure of G-glass is a mixture of low PE core regions (grains) embedded in a surrounding disordered medium with high PE shells. The similar G-glass structure was also observed in a larger system of 256,000 atoms, as shown in Fig. S6(a), indicating that G-glass formation can be well described using 32,000 atoms system. The atomic configurations in Fig. 5(a-c) also reveals that the G-glass consists of separated Cu rich regions and Ag rich regions, respectively. This is consistent with the thermodynamics analysis showing that the physical mixture of crystals is the ground state structure at low T. To determine whether the PE density maps correlate with the chemical separation, we computed the concentrations of the low PE and high PE regions. The lowest PE regions (10% lowest PE atoms) are composed of 6.8% Cu and 93.2%Ag, which is very
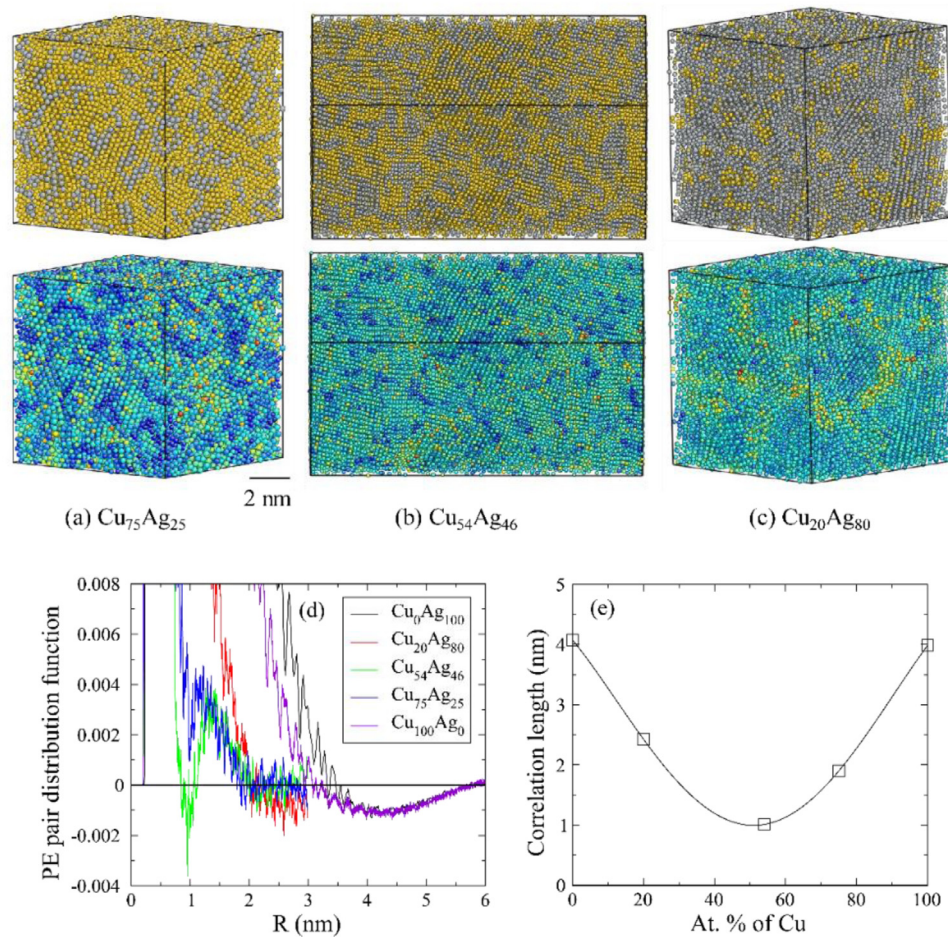
Fig. 5. (a-c) Atomic structures and PE density map of various compositions: $Cu_{75}Ag_{25}$, $Cu_{54}Ag_{46}$, and $Cu_{20}Ag_{80}$. (d) PE pair distribution function of various compositions. The curves of binary systems are smoothed, and the raw data can be found in Fig. S7. (e) The correlation length of PE density for various compositions.

similar to that of the highest PE region (10% highest PE atoms), 7.1% Cu and 92.9% Ag. Therefore, chemical compositions in G-glass are similar in both highest PE and lowest PE regions. However, these compositions differ widely from the average bulk composition of $Cu_{75}Ag_{25}$. This suggests that significant local chemical partitioning (on a scale of 1−2 nm) is required for G-phase nucleation.

The scale of the low PE core regions appears to depend on alloy composition, as illustrated in Fig. 5(a-c). We therefore refer to the length scale of the heterogeneity as $\Lambda(c)$. To investigate the variation of $\Lambda(c)$ with compositions, we computed the PE pair distribution function (PE-pdf) for configurations shown in Fig. 5(a-c). This function illustrates the range of correlation in the atomic PE-density maps. For comparison, we also computed the PE-pdf for the G-phase of the elemental components: Ag and Cu, with the PE density maps and PE-pdf shown in Fig. 6. As shown in Fig. 5(d), the single component G-glasses exhibit a noticeably coarser heterogeneous nanostructure. With the increase in chemical mixing, the $\Lambda(c)$ decreases significantly from 3.99 nm in pure Cu to 1.01 nm at the eutectic composition. Note that there is a small dip at ~1 nm in the PE-pdf curves for the finer scale heterogenous $Cu_{75}Ag_{25}$ structure. This may be in fact related to the chemical heterogeneity in this structure. For the binary systems, we used 32,000 atoms system with the cell length of ~8 nm which is several times larger than $\Lambda(c)$. The comparison with a larger system of 256,000 atoms system, displayed in Fig. S6(b), indicated that the $\Lambda(c)$ is the same for two systems with different sizes, suggesting that it is reliable to obtain $\Lambda(c)$ using 32,000 atom systems. For elemental Ag and Cu systems, we used still larger supercells of 2,048,000 atoms (~32 nm cell size), as shown in Fig. 6. As $\Lambda(c)$ were computed for various compositions, we established a relationship
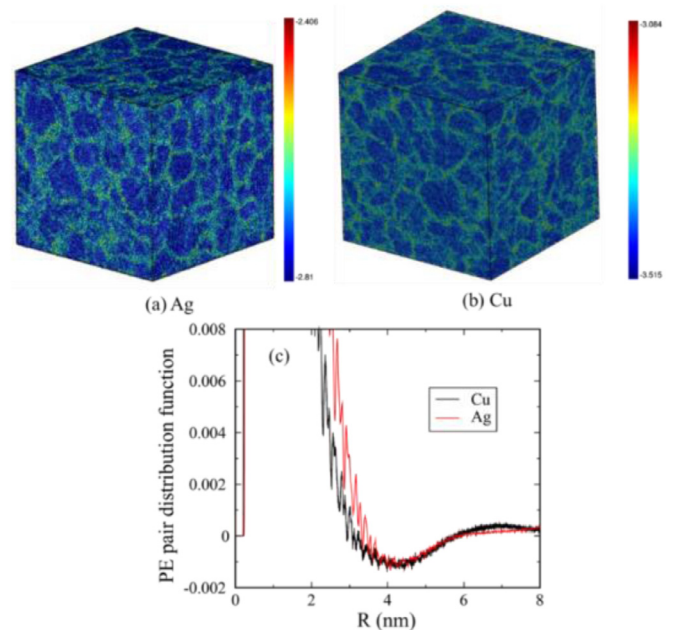

Fig. 6. The PE density map and PE-pdf of elemental Ag and Cu systems with 2,048,000 atoms: (a,b) PE density map of Ag (a) and Cu(b); (c) The PE-pdf for Ag and Cu, respectively.

between correlation length $\Lambda(c)$ and composition, as shown in Fig. 5 (e). The $\Lambda(c)$ shows a clear correlation with both composition and the latent heat of the L-G transition in Fig. 4(a), suggesting that chemical mixing both decreases the $\Lambda(c)$ and therefore suppress the driving force for the L-G transition. This provides a possible explanation as to why the G-glass is rarely observed in atomistic simulations of good glass forming liquids since most of these studies focused on near eutectic MGs, such as the Cu-Zr [40] and Pd-Si [41] systems, where the latent heat of the L-G transition is expected to be quite small and the nucleation of the G-phase will thus tend to be suppressed by a small thermodynamic driving force for the L-G transition.

3.4. Discussion of heterogenous characteristics of G-phase and L-G coexistence

The metastable G-phase exhibits a heterogenous structure with local isolated ordered core regions embedded and surrounded by a disordered liquid-like matrix. The fact that the ordered cores are isolated, mutually uncorrelated, and do not form a continuous network makes the G-phase a glass phase without long range order. The absence of long range translational order is demonstrated from the XRD plot displayed in Fig. S2 of SM. The local ordered cores exhibit short-range order, but they also exhibit curved atomic planes, stacking faults, point defect clusters, and other features indicating they are not equilibrium crystals. The ordered cores are in metastable equilibrium with a surrounding liquid-like matrix and do not grow, even on heating to elevated temperatures, as indicated from the L-G coexistence simulations displayed in Fig. 1. In addition, the HA analyses, displayed in Fig. 3, show that there are only ~20% fcc+hcp atoms in the G-phase. The crystalline fcc+hcp atoms comprise a small minority in the G-phase and are localized into separated clusters.

The absence of long-range order defines a glassy state. Local order in the G-phase is spatially limited to the typical radius (~1.0 nm) of the ordered core regions. Neighboring core regions are surrounded by and separated by a continuous network of liquid-like matrix. The ordered core cores are spatially uncorrelated (or incoherent) with each other. There is therefore no long range order on the scale of the simulation cell. It is this feature that makes glassy description applicable.

In addition, the metastable G-phase glass is expected to remain stable over relatively long time scales, We did not observe growth or coarsening of the ordered core regions in MD simulations of over 10 ns. Furthermore, our coexistence simulations (Fig. 1) suggest that the interface between the L-phase and G-phase also remains stable up to $T_{G,M}$. Our previous study on pure Ag G-phase [36] demonstrates that the free energy of the order core regions is not significantly different from that of the disorder regions. It follows that there is no thermodynamics apparent driving force for the growth of the core regions. One therefore expects G-phase structure to be relatively stable upon aging.

The G-phase formation was observed at 700 K in our MD simulations that are limited to sub 100 ns. At higher temperatures above 700 K but lower than $T_{G,M}$, it is expected that G-phase formation will occur if the liquid persists for longer times. The $T_{G,M}$ for $Cu_{75}Ag_{25}$ was derived to be ~875 K from two-phase simulations, which is lower than the $T_{X,M}$ of 1050 K. Therefore, G-phase formation is to be expected to occur below $T_{G,M}$ if crystallization is avoided during the process. It is worth noting that the $T_{G,M}$ determined here is only valid for the timescale over which the G-phase remains stable. The G-phase could well transform to lower energy states with higher $T_{G,M}$ given sufficient waiting time.

The heterogenous structure of G-phase resembles that of so called "nanocrystalline" materials. Technically, a nanocrystal is defined as a crystalline particle of size is less than 100 nanometers. The correlation length of our G-phase various systematically with composition decreasing from several nm's in the elemental metals to ~1 nm at the eutectic composition, as shown in Fig. 5e. This suggests the size of the ordered core regions in the G-phase may even fall below 1 nm in

a multicomponent eutectic alloy or a deeper binary eutectic alloy. Obviously, there is a length scale below which the notion of a crystal loses meaning. Finally, it is noted that these ordered core regions are not actually ordered crystals, but contain highly curved planes, stacking faults, and other extended and point defects.

The present G-phase exhibits a pronounced nano-scale spatial heterogeneity with locally ordered crystal-like core regions surrounded by disordered liquid-like regions. Similar structures have been reported in a very recent MD study where the heterogeneous micro-structures form following very extended, ~80 μs, MD simulations of a binary Lennard-Jones system [49]. The underlying physics of this L-G transition needs to be explored further for understanding the fundamentals of metallic glass formation.

3.5. Discussion of elastic rigidity of glass transition

Long-range elasticity plays an essential role in the glass transition [12]. To illustrate the possible underlying physical origin of the L-G transition, we computed the shear modulus of liquid (L), L-glass, and G-glass as a function of temperature for composition $Cu_{75}Ag_{25}$. The shear modulus of various phases is displayed in Fig. 7. For the L phase above 1000 K, the shear modulus is close to zero as expected since a high temperature liquid should exhibit no persistent shear rigidity. In contrast, the L-glass and G-glass both exhibit a persistent finite shear modulus on the MD timescale of ns's below the T_g. The shear modulus of the L-glass exhibits a gradual and continuous increase from the liquid as the temperature decreases from 900 K to 600 K, indicating that the structure of L-glass is inherently that of a liquid phase. However, the shear modulus of the G-glass shows an abrupt increase by ~8 GPa compared to L-glass, which provides strong evidence for the first order character of the L-G transition. As temperature decreases below the freezing transition, the difference in the shear moduli between the G-phase and the L-phase becomes smaller. Both G-glass and L-glass shows a linear increase in shear modulus in low temperature below freezing due to the expected Debye−Grüneisen behavior. The slope vs. T of the shear modulus in both glasses is close to that for the crystalline solid, as shown in Fig. 7.

The significant increase of shear modulus for the G-glass vs. L-glass suggests that the configurational rearrangements in the G-glass are constrained by additional long-range elastic fields. Such constraints on configurational excitation of the G-glass reduce its configurational entropy compared to the liquid or L-glass. This is consistent with the entropy drop during the L-G transition, as shown in Fig. 4(c). Thus, the G-glass is further distinguished from the L-glass by the emergence of stronger
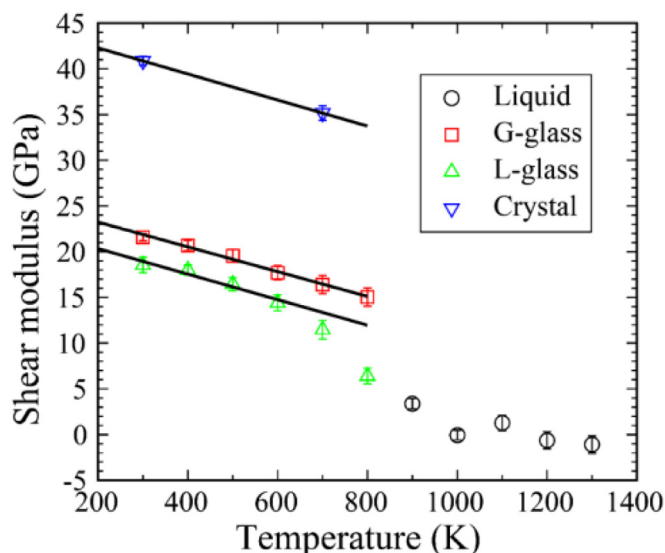

Fig. 7. Shear modulus of various phases with the composition of $Cu_{25}Ag_{75}$.

elastic rigidity, with a larger shear modulus. We suggest that the discontinuous jump in global rigidity for the G-glass is related to long-range elastic interactions between local configurational excitations [50]. The driving force for G-glass formation from the L-glass is likely related to these elastic long-range interactions.

4. Summary

In summary, we examined the glass transition in binary Cu-Ag liquids and identified two different glass phases: L-glass and G-glass. The G-glass, frozen from the supercooled liquids at isothermal MD simulations, exhibits the character of a first order phase transition with finite latent heat, entropy jump, and reversibility. The G-glass is a metastable heterogenous phase consisting of low PE core regions fully embedded in a surrounding disordered medium with high PE. In contrast, the L-glass, obtained from the direct quench simulations, exhibits more homogeneous character, more like most glass phases in most previous MD studies. The chemical mixing in the binary Cu-Ag systems decreases the characteristic length scale of low PE regions, suppressing the G-glass nucleation, leading to a small latent heat. By analyzing the shear modulus of various phases, we conclude that the first order L-G transition may arise from the long-range elastic field due to the interactions of configurational excitations.

Declaration of Competing Interests

The authors declare no competing financial interests.

Acknowledgments

Supplementary materials

Supplementary material associated with this article can be found in the online version at doi:10.1016/j.actamat.2020.05.060.

References

[1] D. Tabor, Gases, Liquids, and Solids (and Other States of Matter), Cambridge University Press, Cambridge, U.K., 1991.
[2] C.A. Angell, Formation of glasses from liquids and biopolymers, Science 267 (1995) 1924–1935.
[3] W.L. Johnson, Bulk glass-forming metallic alloys: science and technology, MRS Bull 24 (1995) 42–56.
[4] Q. An, L.Q. Zheng, S.N. Luo, Vacancy-induced densification of silica glass, J. Non-Cryst. Solids 352 (2006) 3320–3325.
[5] J.D. Ferry, Viscoelastic Properties of Polymers, John Wiley & Sons Inc., New York, USA., 1961.
[6] W. Kauzmann, The nature of the glassy state and the behavior of liquids at low temperatures, Chem. Rev. 43 (1948) 219–256.
[7] W. Klement Jr., R.H. Willens, P. Duwez, Non-crystalline structure in solidified gold−silicon Alloys, Nature 187 (1960) 869–870.
[8] P. Duwez, R.H. Willens, R.C. Crewdson, Amorphous phase in palladium−silicon alloys, J. Appl. Phys. 36 (1965) 2267–2269.
[9] H.S. Chen, D. Turnbull, Thermal evidence of a glass transition in gold-silicon-germanium alloy, Appl. Phys. Lett. 10 (1967) 284–286.
[10] A.L. Greer, Metallic glasses, Science 267 (1995) 1947–1953.
[11] A. Inoue, Stabilization of metallic supercooled liquid and bulk amorphous alloys, Acta Mater. 48 (2000) 279–306.
[12] M. Goldstein, Viscous liquids and glass transition − a potential energy barrier picture, J. Chem. Phys. 51 (1969) 3728–3739.
[13] F.H. Stillinger, P.G. Debenedetti, Glass transition thermodynamics and kinetics, Ann. Rev. Condens. Matter Phys. 4 (2013) 263–285.
[14] P.G. Debenedetti, F.H. Stillinger, Supercooled liquids and the glass transition, Nature 410 (2001) 259–267.
[15] F. Sciortino, W. Kob, P. Tartaglia, Inherent structure entropy of supercooled liquids, Phys. Rev. Lett. 83 (1999) 3214–3217.
[16] L.M. Martinez, C.A. Angell, A thermodynamic connection to the fragility of glass-forming liquids, Nature 410 (2001) 663–667.
[17] D.J. Wales, Energy Landscapes: Applications to Clusters, Biomolecules, and Glasses, Cambridge University Press, Cambridge, U.K., 2004.
[18] Z.H. Yang, Y. Fujii, F.K. Lee, C.H. Lam, O.K.C. Tsui, Glass transition dynamics and surface layer mobility in unentangled polystyrene films, Science 328 (2010) 1676–1679.
[19] P.G. Debenedetti, Metastable Liquids, Princeton University Press, Princeton, U.S.A., 1996.
[20] M.D. Ediger, Spatially heterogeneous dynamics in supercooled liquids, Ann. Rev. Phys. Chem. 51 (2000) 99–128.
[21] O. Mishima, Y. Suzuki, Propagation of the polyamorphic transition of ice and the liquid-liquid critical point, Nature 419 (2002) 599–603.
[22] M. Zhu, J.Q. Wang, J.H. Perepezko, L. Yu, Possible existence of two amorphous phases of D-mannitol related by a first order phase transition, J. Chem. Phys. 142 (2015) 244504.
[23] L. Cohen, A. Ha, X. Zhao, M. Lee, T. Fischer, J.J. Strouse, D. Kevelson, A low-temperature amorphous phase in a fragile glass-forming substance, J. Phys. Chem. 100 (1996) 8518–8526.
[24] P.F. McMillan, M. Wilson, D. Daisenberger, D. Machon, A density-driven phase transition between semiconducting and metallic polyamorphs of silicon, Nat. Mater. 4 (2005) 680–684.
[25] Y. Katayama, K. Tsuji, X-ray structural studies on elemental liquids under high pressures,, J. Phys. 15 (2003) 6085–6103.
[26] G. Monaco, S. Falconi, W.A. Crichton, M. Mezouar, Nature of the first-order phase transition in fluid phosphorus at high temperature and pressure, Phys. Rev. Lett. 90 (2004) 255701.
[27] W. Way, P. Wadhwa, R. Busch, The influence of shear rate and temperature on the viscosity and fragility of Zr-Ti-Cu-Ni-Be metallic glass-forming liquid, Acta Mater 55 (2007) 2977–2983.
[28] H.W. Sheng, H.Z. Liu, Y.Q. Cheng, J. Wen, P.L. Lee, W.K. Luo, S.D. Shastri, E. Ma, Polyamorphism in a metallic glass, Nat. Mater. 6 (2007) 192–197.
[29] J.J.Z. Li, W.K. Rhim, C.P. Kim, K. Samwer, W.J. Johnson, Evidence of a liquid-liquid phase transition in metallic fluids by electrostatic levitation, Acta Mater 59 (2011) 2166–2171.
[30] K.L. Kearns, M.D. Ediger, H. Heiko, C. Schick, One micrometer length scale controls kinetic stability of low-energy glasses, J. Phys. Chem. Lett. 1 (2010) 388–392.
[31] K. Dawson, L.A. Kopff, L. Zhu, R.J. McMahon, L. Yu, R. Richert, M.D. Ediger, Molecular packing in highly stable glasses of vapor-deposited tris-naphthylbenzene isomers, J. Chem. Phys. 136 (2012) 094505.
[32] S.S. Dalal, M.D. Ediger, Molecular orientation in stable glasses of indomethacin, J. Phys. Chem. Lett. 3 (2012) 1229–1233.
[33] Y. Guo, A. Morozov, D. Schneider, J.W. Chung, C. Zhang, M. Waldmann, N. Yao, G. Fytas, C.B. Arnold, R.D. Priestley, Ultrastable nanostructured polymer glasses, Nat. Mater. 11 (2012) 337–343.
[34] J.E.K. Schawe, J.F. Löffler, Existence of multiple critical cooling rates which generate different types of monolithic metallic glass, Nat. Commun. 10 (2019) 1337.
[35] H. Tong, H. Tanaka, Revealing hidden structural order controlling both fast and slow glassy dynamics in supercooled liquids, Phys. Rev. X 8 (2018) 011041.
[36] Q. An, W.L. Johnson, K. Samwer, S.L. Corona, W.A. Goddard III, First-order phase transition in liquid Ag to the heterogeneous G-phase, J. Phys. Chem. Lett. 11 (2020) 632–645.
[37] K. Samwer, R. Busch, W.L. Johnson, Change of compressibility at the glass transition and prigogine-defay ratio in ZrTiCuNiBe alloys, Phys. Rev. Lett. 82 (1999) 580–583.
[38] S. Plimpton, Fast parallel algorithms for short-range molecular dynamics, J. Comp. Phys. 117 (1995) 1–19.
[39] P.L. Williams, Y. Mishin, J.C. Hamilton, An embedded-atom potential for the Cu−Ag system, Model. Simul. Mater, Sci. Eng. 14 (2006) 817–833.
[40] Q. An, L.Q. Zheng, R.S. Fu, S.D. Ni, S.N. Luo, Solid−liquid transitions of sodium chloride at high pressures, J. Chem. Phys. 125 (2006) 154510.
[41] J.D. Honeycutt, H.C. Andersen, Molecular dynamics study of melting and freezing of small lennard-jones clusters, J. Phys. Chem. 91 (1987) 4950–4963.
[42] R. Hill, The elastic behaviour of a crystalline aggregate, Proc. Phys. Soc., London, Sect. A 65 (1952) 349–354.
[43] Y. Le Page, P. Saxe, Symmetry-general least-squares extraction of elastic data for strained materials from ab initio calculations of stress, Phys. Rev. B 65 (2002) 104104.
[44] T.B. Massalski, Binary Alloy Phase Diagrams, ASM, Materials Park, OH, 1986.
[45] Q. An, K. Samwer, W.A. Goddard III, W.L. Johnson, A. Jaramillo-Botero, G. Garret, M.D. Demetriou, Predicted optimum composition for the glass-forming ability of bulk amorphous alloys: application to Cu−Zr−Al, J. Phys. Chem. Lett. 3 (2012) 3143–3148.
[46] Q. An, K. Samwer, M.D. Demetriou, M.C. Floyd, D.O. Duggins, W.L. Johnson, W.A. Goddard III, How the toughness in metallic glasses depends on topological and chemical heterogeneity, Proc. Nat. Acad. Sci. U S A 113 (2016) 7053–7058.
[47] G. Williams, D.C. Watts, Non-symmetrical dielectric relaxation behavior arising from a simple empirical decay function, Trans. Faraday Soc. 66 (1970) 80–85.
[48] R. Najafabadi, D.J. Srolovitz, E. Ma, M. Atzmon, Thermodynamic properties of metastable Ag-Cu alloys, J. Appl. Phys. 74 (1993) 3144–3149.
[49] P.M. Derlet, R. Maaß, Emergent structural length scales in a model binary glass − The micro-second molecular dynamics time-scale regime, J. Alloys Compd 821 (2020) 153209.
[50] J.D. Eshelby, The determination of the elastic field of an ellipsoidal inclusion, and related problems, Proc. Royal Soc. 241 (1957) 376–396.